PAPER

Check for updates

Formaldehyde gas sensor with extremely high response employing cobalt-doped SnO₂ ultrafine nanoparticles†

Shiqiang Zhou,‡[ab] Huapeng Wang,‡[a] Jicu Hu,‡[a] Tianping Lv,[a] Qian Rong,[a] Yumin Zhang,[a] Baoye Zi,[a] Mingpeng Chen,[c] Dongming Zhang,[a] Jun Wei,[b] Jin Zhang*[a] and Qingju Liu [ID] *[a]

Formaldehyde is a common carcinogen in daily life and harmful to health. The detection of formaldehyde by a metal oxide semiconductor gas sensor is an important research direction. In this work, cobalt-doped SnO₂ nanoparticles (Co-SnO₂ NPs) with typical zero-dimensional structure were synthesized by a simple hydrothermal method. At the optimal temperature, the selectivity and response of 0.5% Co-doped SnO₂ to formaldehyde are excellent (for 30 ppm formaldehyde, $R_a/R_g = 163\,437$). Furthermore, the actual minimum detectable concentration of 0.5%Co-SnO₂ NPs is as low as 40 ppb, which exceeds the requirements for formaldehyde detection in the World Health Organization (WHO) guidelines. The significant improvement of 0.5%Co-SnO₂ NPs gas performance can be attributed to the following aspects: firstly, cobalt doping effectively improves the resistance of SnO₂ NPs in the air; moreover, doping creates more defects and oxygen vacancies, which is conducive to the adsorption and desorption of gases. In addition, the crystal size of SnO₂ NPs is vastly small and has unique physical and chemical properties of zero-dimensional materials. At the same time, compared with other gases tested, formaldehyde has a strong reducibility, so that it can be selectively detected at a lower temperature.

1. Introduction

With the aggravation of environmental pollution, the detection of harmful gases has become a vital research field. The WHO guidelines determine that the concentration of formaldehyde in indoor living areas should not exceed 82 ppb.[1] Therefore, it is important to detect formaldehyde efficiently and accurately. Metal oxide gas sensors are widely studied because of their portability and low cost.[2–4] In the case of metal oxide gas sensors, zero-dimensional metal oxide materials (such as quantum dots,[5] nanoparticle clusters[6]) are attracting attention for their unique high gas sensitivity and other superior physical or chemical properties.

Oxygen molecules in the air are adsorbed on the surface of metal oxides to generate adsorbed oxygen, thereby forming

[a]Yunnan Key Laboratory for Micro/Nano Materials & Technology, National Center for International Research on Photoelectric and Energy Materials, School of Materials and Energy, Yunnan University, Kunming 650091, P. R. China. E-mail: qjliu@ynu.edu.cn; zhj@ynu.edu.cn

[b]Shenzhen Key Laboratory of Flexible Printed Electronics Technology Center, Harbin Institute of Technology, Shenzhen University Town, Shenzhen, 518055, China

[c]Institute of Applied Physics and Materials Engineering, University of Macau, Macau SAR, China

† Electronic supplementary information (ESI) available. See DOI: 10.1039/d1na00625h

‡ These authors contributed equally to this work.

a depletion layer on the surface of the materials. According to a momentous characteristic,[7] when the grain size of the zero-dimensional metal oxide is less than or close to two times of the thickness of the depletion layer, the gas sensitivity of the material will be greatly enhanced. The SnO₂ ultrafine nanoparticles are typical zero-dimensional materials and are commonly used in the study of gas sensors,[8] supercapacitors[9] and batteries.[10] Zhu et al.[11] synthesized SnO₂ quantum dots with a size of 2–4 nm by using microwave assisted method, the sensor made by counterpart had a response value of 215 to 300 ppm ethanol, but did not show its selectivity. Du et al.[12] used the conventional hydrothermal synthesis method to prepare SnO₂ quantum dots, and controlled the grain size of the quantum dots by regulating the addition amount of hydrazine. Among them, TQD-1 (average particle size 2.5 nm) revealed a high response to 100 ppm of triethylamine at 240 °C. Nevertheless, its selectivity was poor, and ethanol was the most serious interfering gas.[11–13]

Although the pure SnO₂ zero-dimensional materials in the gas sensor show higher response, there are still some shortcomings, which mainly highlight that the ultra-fine nanoparticles enhance the activity of the materials, leading to the instability of electrical resistance and poor selectivity to various gases, etc. Therefore, researchers are committed to improving sensor performance through various methods. Noble metal functionalization,[14] constructing heterojunctions[15] and element doping[16] can usually improve the gas sensing performance of

the sensor. Noteworthy, doping with metal impurities is one of the most effective ways to increase surface crystal lattice defect and oxygen vacancies, which could to improve the gas sensing properties.[17] Wang et al.[18] demonstrated that SnO_2 composites by doped with Ce-dopant could improve gas sensing properties to ethanol, which could be attributed to the unique advantages of Ce elemental doping. Gu and co-workers[19] have obtained the In and Au doped SnO_2 inverse opal thin films, which enhanced the sensing properties with a response of 308 to 100 ppm of ethanol compared with the pure SnO_2. Moreover, the optimum operating temperature was decreased from 350 °C to 250 °C, and the response/recovery time was shortened obviously by 0.25% Au doping. They indicated that the doping of In and Au contributed to the increase of the adsorbed oxygen amounts which benefited the enhancement of the sensing performance. As a transition metal, Co was used as effective substitute and also for improving gas sensing properties. Chen et al.[20] investigated properties of formaldehyde and acetone sensors based on Co-doped SnO_2 with significant enhancement in the gas sensing performance by the elevation of the Fermi level and the narrowing of the band gap effect. Wang et al.[17] have synthesized Co-doped In_2O_3 nanorods, and the enhancement of the gas response was attributed to the incorporation of Co, which suggested the important role of the amount of oxygen vacancies and adsorbed oxygen in enhancing sensing performance of In_2O_3 sensors. Therefore, Co-doped SnO_2 are expected to enhance the gas sensing properties.

In this study, cobalt doping was used to improve the gas properties of SnO_2 nanoparticles (SnO_2 NPs), which is simple and low-cost to prepare and can retain the unique physical and chemical properties of SnO_2 zero-dimensional materials. Cobalt-doped SnO_2 NPs (Co-SnO_2 NPs) have been successfully synthesized and the research results demonstrate that the sensing performance can be effectively enhanced by adjusting the grain size and resistance of SnO_2 via controlling the cobalt doping ratio. Furthermore, the gas sensor based on 0.5% cobalt-doped SnO_2 nanoparticles (0.5%Co-SnO_2 NPs) is also determined to achieve optimum gas performance at 30 ppm formaldehyde and operating temperatures as low as 90 °C, which shows incredible response, whose value is as high as 163 437. This value is nearly 220 times higher than that of pure SnO_2 NPs, and 0.5%Co-SnO_2 NPs also exhibits inconceivable selectivity thus it has a high application potential.

2. Experimental sections

2.1 Chemical agents

Stannic chloride ($SnCl_4 \cdot 5H_2O$), cobaltous nitrate hexahydrate ($Co(NO_3)_2 \cdot 6H_2O$), hydrazine hydrate ($N_2H_4 \cdot H_2O$, 80%), were purchased from Aladdin Bio-Chem Technology Co. Ltd. All chemicals are analytical grade and can be used directly without further purification. The solvent is deionized water.

2.2 Synthesis process

Preparation of SnO_2 nanoparticles (SnO_2 NPs). The preparation method of SnO_2 nanoparticles is similar to the reported,[21] but with some changes. In a typical experiment, SnO_2 NPs are prepared by one-step hydrothermal method. Hydrothermal experiments are carried out at relatively low temperatures. First, 1.9689 g of $SnCl_4 \cdot 5H_2O$ was dissolved in 100 ml of deionized water and stirred at room temperature for 10 minutes. Next, 2.81 ml of hydrazine hydrate (80%) was dropped into the solution and stirred at room temperature for 30 minutes. The prepared solution was transferred to a 150 ml Teflon-lined stainless steel autoclave and then heated at 100 °C for 18 hours. After cooling to room temperature, the product was centrifuged and washed several times with deionized water. The resulting samples were dispersed in a small amount of deionized water and then freeze-dried. Finally, the dried samples were annealed at 350 °C for 2 hours to obtain SnO_2 NPs.

Preparation of Co doped SnO_2 nanoparticles (Co-SnO_2 NPs). The preparation method of Co-SnO_2 NPs is similar to that of SnO_2 NPs, except that the corresponding number of $SnCl_4 \cdot 5H_2O$ is replaced by 0.5 at%, 1 at% and 2 at% of Co $(NO_3)_2 \cdot 6H_2O$. The $Co(NO_3)_2 \cdot 6H_2O$ and $SnCl_4 \cdot 5H_2O$ were added to deionized water together, and the other steps were identical. Three samples prepared by adding different proportions of $Co(NO_3)_2 \cdot 6H_2O$ were named 0.5%Co-SnO_2 NPs, 1%Co-SnO_2 NPs, 2%Co-SnO_2 NPs, respectively.

2.3 Characterization of materials

The crystal structures of the samples were analyzed by X-ray diffraction with Cu Kα1 radiation ($\lambda = 1.54059$). The Raman spectrum was measured from 100 to 900 cm^{-1} (inVia reflex Raman spectrometer, laser radiation: $\lambda = 532$ nm). The chemical composition and elemental valence of the materials were examined by X-ray photoelectron spectroscopy (XPS) (K-Alpha spectrometer, Thermo Fisher Scientific Co. Ltd) with Al Kα excitation (1486.6 eV). The particle size and elemental mapping of the prepared samples were observed using a TEM (Tecnai G^2 TF30 S-Twin transmission electron microscope with an acceleration voltage of 300 kV). The surface area was measured by the nitrogen adsorption isotherm using the Brunauer–Emmett–Teller (BET) method, and the pore size distribution was estimated by the Barrett–Joyner–Halenda (BJH) method. The steady-state photoluminescence (PL) emission spectra are obtained by direct detection of powder samples via a fluorescence spectrometer (FL4500, Japan) with excitation wavelength of 325 nm. The electron spin resonance (EPR) spectroscopy was performed on Bruker EMX to detect the unpaired electrons of samples powder at 100 K (the EPR signals are poor at room and higher temperatures for the cobalt ion due to very short spin-lattice relaxation times which broaden the lines considerably, making it difficult to study the temperature variation of cobalt spectrum).

2.4 Fabrication and measurement of gas sensors

The sensor used in the experiment is thick film type. A platinum circuit is plated on the surface of the rectangular ceramic substrate, and two electrodes are formed on the bottom of the substrate. Through these two electrodes, the test device (SD-101

gas sensing performance testing device, Wuhan Huachuang Ruike Tech. Co. Ltd., Wuhan, China) can control the test temperature by regulating the heating power. In this experiment, the prepared sample was mixed with printing oil in a mass ratio of 1 : 1 and ground uniformly. Then the paste was printed on the circular area on the top of the sensor by screen printing technique. Finally, the prepared sensors were annealed in the muffle furnace for 2 hours. The sensing properties were evaluated by HCRK-SD101 static gas distribution system (Fig. S1,† Wuhan HCRK Technology Co. Ltd.). The prepared sensors were installed in the test chamber (2.7 L) and then and inject a quantitative liquid (calculation of the concentration when the organic volatile liquid is converted into gaseous VOCs) into the evaporator of the closed chamber to produce a corresponding concentration of gas. Humidity control is to pass atomized water vapor into the cavity. The instrument has a humidity detection function, and the test is performed after the humidity in the cavity is relatively stable. In this work, the response is defined as $S = R_a/R_g$ (n-type semiconductor), where R_a represents the resistance of the device in the air and R_g represents the resistance of the sensor in the target gas. And the response time and recovery time are defined as the time required for 90% of the total resistance change during gas adsorption and desorption, respectively. Unless otherwise noted, all tests in this article were tested in a dry environment.

3. Results and discussion

3.1 Structural and morphological characteristics

As shown in Fig. 1(a), X-ray diffraction analysis was performed on the four prepared samples to determine the chemical composition and the crystal phase. The purple curve at the bottom of the spectrum represents pure SnO_2 NPs, and it can be seen that all the peaks of the curve correspond to the standard PDF card (JCPDS 71-0652). The other three samples contained 0.5%, 1%, and 2% molar ratio of cobalt, are similar to pure SnO_2 NPs, no significant Co_3O_4 or other Co-containing compounds, such as CoO, are found. Therefore, it can be inferred that cobalt

is doped into the SnO_2 NPs crystal. In addition, as shown in Fig. 1(b), a high angle shift was detected from the (110) peak via comparing the Co-doped SnO_2 with pure SnO_2. This could be ascribed to the difference between the radius of Sn^{4+} (0.81 Å) and Co^{2+} (0.72 Å) or Co^{3+} (0.62 Å), confirming that Co is incorporated into the SnO_2 lattice.[22]

Moreover, the average crystallite size of the prepared samples is calculated by using Scherer's equation:

$$D = K\lambda/\beta \cos \theta \tag{1}$$

where D is the crystallite size, K the shape factor ($K = 0.89$), λ is the wavelength of incident X-ray ($\lambda = 0.15406$ nm), β is the full width of the half maximum (FWHM) in radian and θ is the Bragg diffraction angle. The average crystallite size of 0.5%Co-SnO_2 NPs, 1%Co-SnO_2 NPs and 2%Co-SnO_2 NPs is 2.5 nm, 3.1 nm, 3.7 nm, 4.5 nm, respectively. It indicates that the doping of Co would promote the growth of crystallites of the SnO_2. Doping can inhibit crystal growth and can also promote crystal growth. From the perspective of crystal structure, doping will introduce defects, which can be suppressed and can also promote crystal growth. In this experiment, the increase in the average size of the crystal grains can be attributed to the defects introduced by the doping of Co. The grain size and morphology of prepared samples were investigated by TEM to confirm an influence of Co on increasing the size of SnO_2 nanoparticles.

The Raman spectra of the samples are shown in Fig. S2.† It can be seen from XRD analysis that the as-prepared SnO_2 NPs have a typical tetragonal rutile structure, and the corresponding space group is $D_{4h}{}^{14}$ ($P4_2/mnm$). The mechanical representation of the normal modality of the Brillouin zone is as follows:

$$\Gamma = \Gamma_1^+(A_{1g}) + \Gamma_2^+(A_{2g}) + \Gamma_3^+(B_{1g}) + \Gamma_4^+(B_{2g}) + \Gamma_5^-(E_g) \\ + 2\Gamma_1^-(A_{2u}) + 2\Gamma_2^-(B_{1u}) + 4\Gamma_5^+(E_u) \tag{2}$$

Generally, modes A_{1g}, B_{1g}, B_{2g}, and E_g have Raman active, and A_{2u} and E_u have infrared active. The peaks observed at 453.6 and 772.7 cm^{-1} correspond to the E_g and B_{2g} modes,
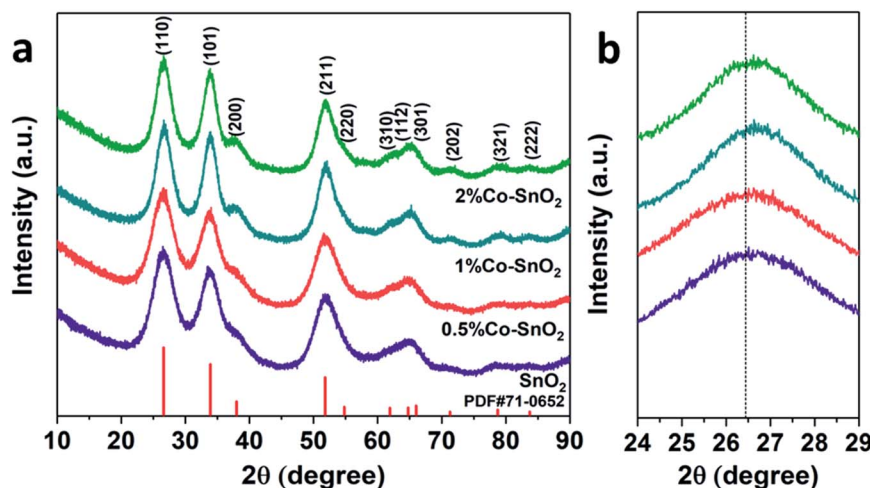

Fig. 1 (a) Full angle range of XRD patterns and (b) high-resolution of (110) peak of the pure, 0.5%, 1% and 2% Co-doped SnO_2 NPs.

respectively. The Raman mode at 623.2 cm^{-1} is assigned to A$_{1g}$. However, as the cobalt content increases, A$_{1g}$ gradually shifts to the high frequency region, and the 2%Co-SnO$_2$ NPs curve shifts to 626.6 cm^{-1}. The vibrational motion represented by the B$_{1g}$ mode is generally only present in single crystal SnO$_2$, which is not common in polycrystals because the intensity is too weak.[23] Similar to the A$_{1g}$ mode, the B$_{1g}$ mode has the same trend, shifting from pure SnO$_2$ NPs (111.0 cm^{-1}) to 2%Co-SnO$_2$ NPs (114.4 cm^{-1}). The peak at 574.5 cm^{-1} (D peak) is the only peak found in ultrafine nanoparticles, which is attributed to the optically inactive A$_{2g}$ mode.[23] In addition, new peaks are observed at 310.9 and 357.9 cm^{-1}, which are assigned to the IR active E$_u$ (TO) and E$_u$ (LO) modes, respectively. This is due to the increase in the disorder rate and the size effect causing the structural change, so the IR modes become weakly active.[24] Interestingly, as the content of cobalt increases, the Raman peak intensity decreases accordingly, which indicates that the doping of cobalt leads to changes in local disorder and defects.[25] And no peaks of the phase of CoO, Co$_3$O$_4$, SnO, *etc.* are observed.

In order to further confirm the composition and valence state of the surface of the samples, XPS detection was carried out. The full spectrum of the samples is shown in Fig. 2(a), which visually shows the existence of the Sn and O peaks. Fig. 2(b) shows the XPS spectrum of Sn. The purple curve represents pure SnO$_2$ NPs with two distinct peaks at 495.0 eV

and 486.7 eV, corresponding to Sn^{4+} 3d$_{3/2}$ and Sn^{4+} 3d$_{5/2}$, respectively.[26,27] Besides, as the proportion of Co doping increases, it can be clearly found that the Sn 3d peak shifts significantly. This further confirms the successful doping of Co. Fig. 2(c) and (d) show high-resolution XPS spectra of Co and O 1s (SnO$_2$ NPs and 0.5%Co-SnO$_2$ NPs), respectively. There are obviously three peaks in the Co 2p$_{3/2}$ diagram, and the peak at 785.8 eV is assigned to the shakeup satellite peak.[28] In addition, the remaining two peaks are attributed to Co^{2+} and Co^{3+}, respectively. The Co^{2+}/Co^{3+} ratio of 0.5%, 1%, 2%Co-SnO$_2$ NPs corresponds to 2.02, 1.64, 1.22, which indicates that the Co^{2+} ratio decreases as the amount of Co incorporation increases.[29–31] The peak of O 1s in Fig. 2(d) reveals the presence and content of various types of oxygen on the surface of SnO$_2$ NPs and 0.5%Co-SnO$_2$ NPs. O 1s can be fitted as three peaks of 530 eV, 531 eV and 532 eV, which are attributed to the lattice oxygen (O 1$_L$) of SnO$_2$, the oxygen vacancy (O 1$_V$) and the adsorbed oxygen (O 1$_C$) on the surface, respectively. Compared with SnO$_2$ NPs, the O 1$_V$ and O 1$_C$ ratio of 0.5%Co-SnO$_2$ NPs is increased, and the proportion of O 1$_L$ gradually decreases, which mainly due to the successful doping of Co. The increase of O 1$_V$ leads to more active sites in the material, thereby improving gas sensing performance. When the doping amount of Co is further increased, the amount of O 1$_V$ is significantly reduced, which may be due to the combination of Co atoms and oxygen vacancies.[32]
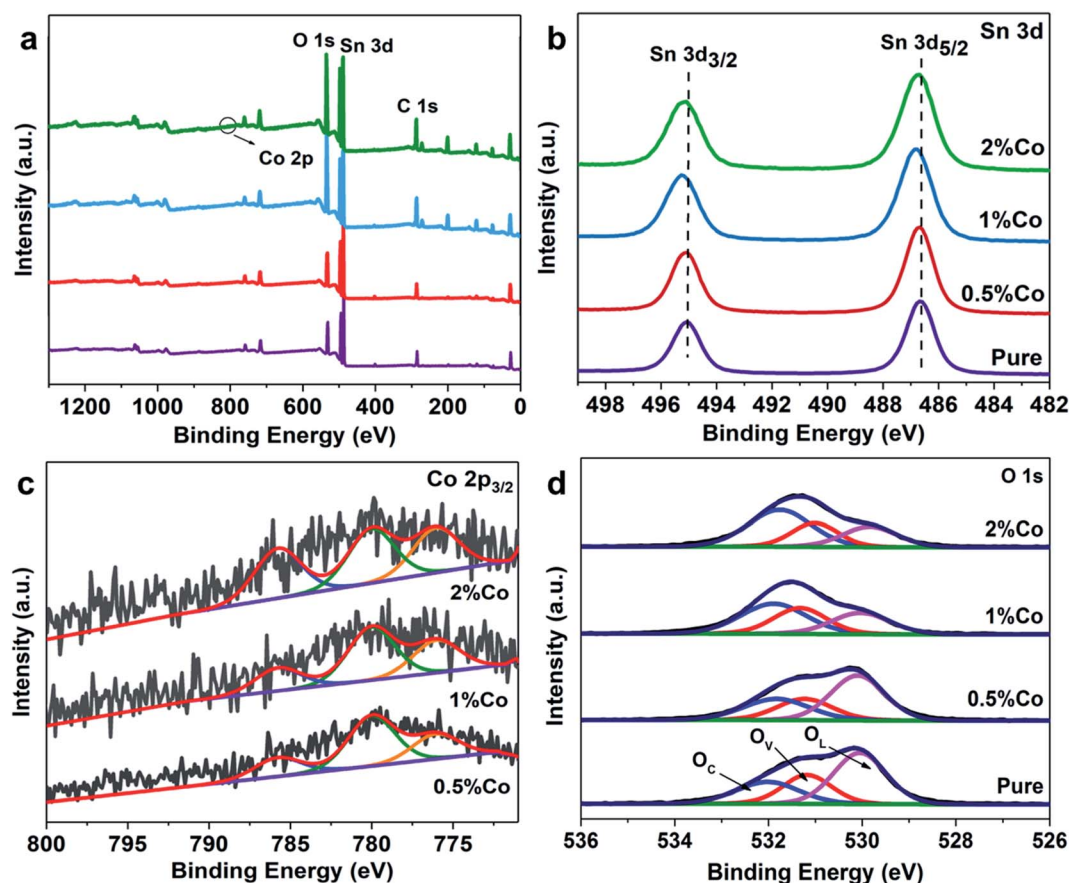

Fig. 2 (a) XPS survey spectra, (b) Sn 3d spectra, (c) Co 2p$_{3/2}$ spectra and (d) O 1s spectra of the pure and Co-doped SnO$_2$ NPs.
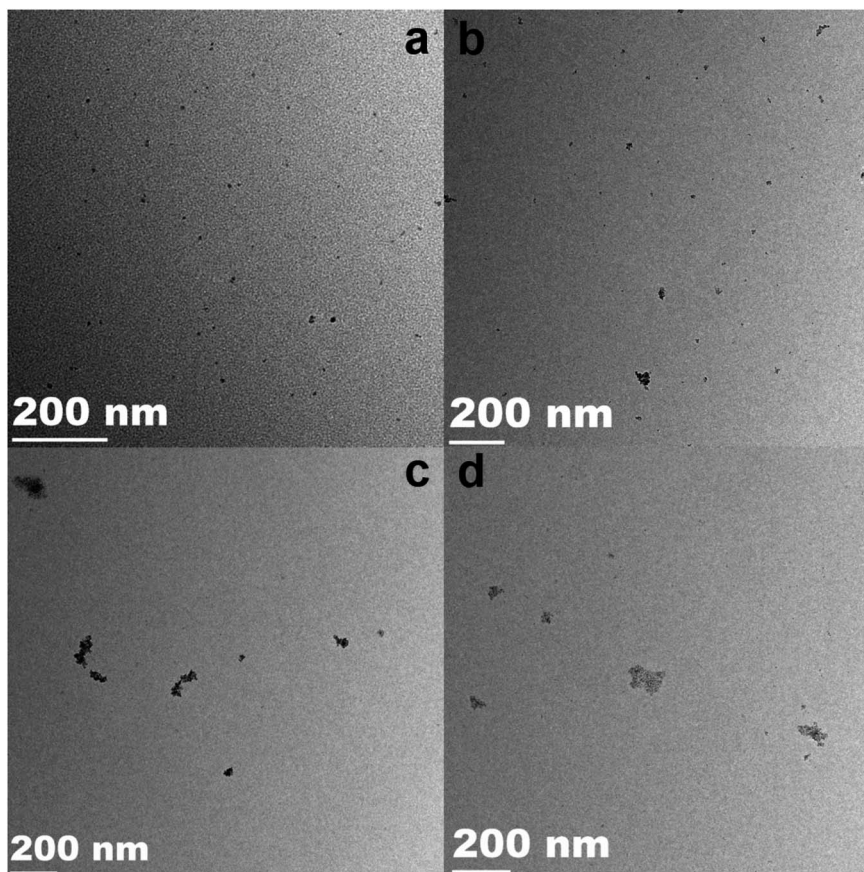
Fig. 3 (a–d) The TEM images of SnO_2 NPs, 0.5%Co-SnO_2 NPs, 1%Co-SnO_2 NPs and 2%Co-SnO_2 NPs.

TEM observations were performed to analyze the structure and distribution of the samples. The TEM images of pure SnO_2 NPs, 0.5%Co-SnO_2 NPs, 1%Co-SnO_2 NPs and 2%Co-SnO_2 NPs are depicted in Fig. 3(a)–(d), which can be clearly found that as the proportion of cobalt increases, the particles become more agglomerated from the comparison of the four images.

And Fig. 4(a)–(d) are the HRTEM images of the corresponding samples. As shown in Fig. 4(a), the interplanar spacing in the lower right inset is 0.265 nm, which corresponds to the (101) lattice plane in the SnO_2 PDF card. In addition, its particle size is only 2.52 nm. The lattice distances are 0.264 nm and 0.332 nm, which correspond to the (101) and (110) crystal faces of SnO_2 in Fig. 4(b)–(d), respectively. In addition, it is extremely obvious that the size of the particles is growing and becoming more agglomerated. The 0.5%Co-SnO_2 NP size is 3.21 nm, whereas 1%Co-SnO_2 NPs and 2%Co-SnO_2 NPs have grown to 4.69 nm and 6.88 nm, respectively. This result is consistent with the Raman analysis.

The prepared all samples were carried out nitrogen adsorption–desorption detection in Fig. 5(a)–(d). With the increase of the amount of cobalt, the sample shows a tendency to close to the H1 hysteresis loops. The surface areas of SnO_2 NPs, 0.5%Co-SnO_2 NPs, 1%Co-SnO_2 NPs and 2%Co-SnO_2 NPs measured by BET are 49.8, 51.6, 60.5 and 72.3 $m^2 \ g^{-1}$, respectively. The increase of specific surface area can provide more adsorption sites, which helps to improve the gas sensing performance. The pore size distribution of each sample is present in the corresponding inset. As can be seen from the inset, cobalt doping has little effect on the pore size distribution of the SnO_2 samples. The large specific surface area contribute to gas diffusion and adsorption of oxygen, thereby improving gas sensing performances.

3.2 Gas-sensing characteristics

Fig. 6(a) exhibits the relationship between temperature and response of gas sensors based on SnO_2 NPs, 0.5%Co-SnO_2 NPs, 1%Co-SnO_2 NPs and 2%Co-SnO_2 NPs at low operating temperature (20–180 °C). And the inset is an enlarged view of the pure SnO_2 NPs and 0.5%Co-SnO_2 NPs curves. Obviously, the response of cobalt-added samples increase significantly compared to pure SnO_2 NPs, and the response of 0.5%Co-SnO_2 NPs is vastly higher than that of other samples. As the temperature increases, the response of 0.5%Co-SnO_2 NPs gradually increases, but starts to decrease after 90 °C. And at the optimum working temperature (90 °C), the response of 0.5%Co-SnO_2 NPs (163 437) is nearly 220 times higher than that of pure SnO_2 NPs (739). Even the 1%Co-SnO_2 NPs has a response value of 33 000 at 90 °C. Thus, the 0.5% Co-SnO_2 NPs highlight the extremely high response to formaldehyde and low operating temperatures, which demonstrates its excellent gas sensing performance.

Fig. 6(b) shows the response and recovery curve of the sensor based on 0.5%Co-SnO_2 NPs to 30 ppm formaldehyde at the
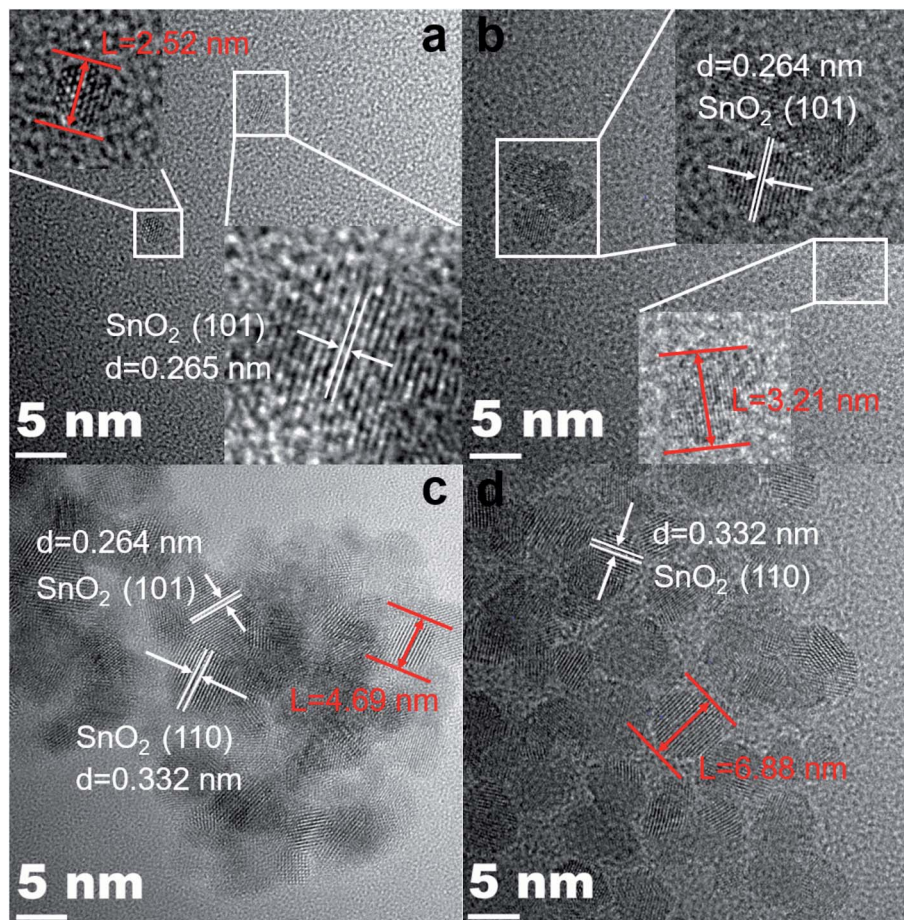
Fig. 4 (a–d) The HRTEM images of SnO₂ NPs, 0.5%Co-SnO₂ NPs, 1%Co-SnO₂ NPs and 2%Co-SnO₂ NPs.

optimum operating temperature, which corresponds to the part marked by the red oval in Fig. 6(c). In this work, the ultra-high response results in long response and recovery times. The response time and recovery time are 652 s and 475 s, respectively. Fig. 6(c) presents the dynamic response and recovery curves of the 0.5%Co-SnO₂ NPs based sensor for different concentrations of formaldehyde at the optimum operating temperature. Obviously, as the concentration of formaldehyde increases, the response of the sensor also increases. For comparison with 0.5%Co-SnO₂ NPs, as shown in Fig. S3,† the gas properties of the remaining three samples at different concentrations of formaldehyde at 90 °C were supplemented. Fig. S3† indicates that although the response of 1%Co-SnO₂ NPs is lower than 0.5%Co-SnO₂ NPs, it is still higher than pure SnO₂ NPs. However, the overall response of 2%Co-SnO₂ NPs is less than that of pure SnO₂ NPs. That is, the response of the sample increases firstly and then decreases with the increase of cobalt ratio. In addition, compared with Fig. 6(c), it can be found that the response and recovery time are increasing with the raise of cobalt content in SnO₂ NPs. Therefore, the gas properties of the sample vary significantly with cobalt doping.

In order to analyze the influence of the material composition change caused by Co doping on the sensor resistance, relevant tests were carried out. Fig. S4(a)† shows that as the temperature

increases, the resistance in air (R_a) of SnO₂ drops rapidly and then tends to be flat. The difference from SnO₂ is that the resistance curves of other samples have changed significantly due to the addition of Co. The R_a curve first increases and then decreases with the increase of temperature. Fig. S4(b)† is the change curves of resistance when the samples adsorb and desorb 30 ppm formaldehyde at 90 °C. The activity of 0.5%Co-SnO₂ NPs is excellent, and the resistance decline trend is the most obvious under the same conditions.

In practical application, the detection standard of formaldehyde is often required to reach the ppb level, so the gas sensing properties of 0.5%Co-SnO₂ NPs are tested under ultra-low concentration of formaldehyde. Fig. 7(a) depicts the transient response curve of 0.5%Co-SnO₂ NPs from 1 ppm to 40 ppb of formaldehyde at the optimum operating temperature of 90 °C. It can be found that the sensor has a high response of 294 even when exposed to formaldehyde gas with a concentration of 40 ppb. This indicates that 0.5%Co-SnO₂ NPs is of high practical value. Moreover, in order to further determine its application value, the limit of detection (LOD) that the sensor can achieve is analyzed from the theoretical level, and the corresponding calculation process is found in the ESI.† And by calculation, the limit of detection is 0.0001 ppb. The results of gas sensitivity test and theoretical calculation show that the
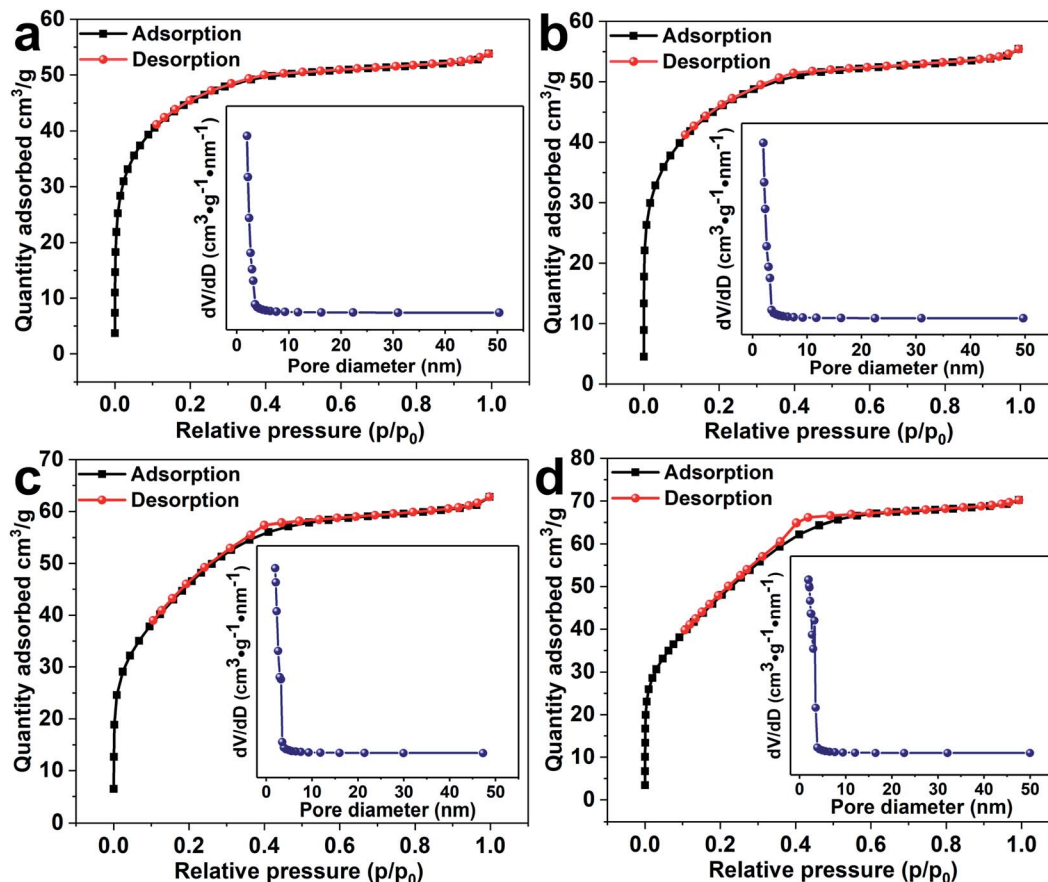
Fig. 5 Nitrogen adsorption–desorption isotherms and corresponding pore size distribution (inset) of (a) SnO$_2$ NPs, (b) 0.5%Co-SnO$_2$ NPs, (c) 1% Co-SnO$_2$ NPs and (d) 2%Co-SnO$_2$ NPs.

0.5%Co-SnO$_2$ NPs has excellent performance. In addition, the long-term stability curve of the 0.5%Co-SnO$_2$ NPs is depicted in Fig. 7(b). The test is conducted every two days for 15 days under conditions of 30 ppm formaldehyde and 90 °C. It is clear that within 15 days, the response change does not exceed 3.1%, which reflects the excellent long-term stability of the 0.5%Co-SnO$_2$ NPs. The excellent long-term stability of 0.5%Co-SnO$_2$ is mainly due to Co doping.[17]

It is well known that the ability to selectively detect a particular gas is an important requirement for the practical application of the sensor. Thus, the responses of four sensors to various gases are compared at 90 °C and 30 ppm as shown in Fig. 8(a)–(d) to assess their selectivity.

In Fig. 8(a), when the SnO$_2$ NPs is exposed to 30 ppm of various gases, it has high response to several gases. The response values of xylene and benzene are 384 and 72.9, respectively. Therefore, the selectivity of SnO$_2$ NPs is poor, and the ratio of $S_{(formaldehyde)}/S_{(xylene)}$ is only 1.92. The selectivity of the 2%Co-SnO$_2$ NPs shown in Fig. 8(d) is improved. The strongest disturbing gas is ethanol with a response value of 7.4, besides the ratio of $S_{(formaldehyde)}/S_{(ethanol)}$ is also raised to 91.9. Nevertheless, the selectivity of the 0.5%Co-SnO$_2$ NPs and the 1%Co-SnO$_2$ NPs is more prominent. In Fig. 8(c), the response of 1%Co-SnO$_2$ NPs to gases other than formaldehyde is only 2.16.

The best selectivity is 0.5%Co-SnO$_2$ NPs, and the $S_{(formaldehyde)}/S_{(xylene)}$ ratio is raised to an incredible degree (16 902), even exceeding the ratio of $S_{(formaldehyde)}/S_{(ethanol)}$ (15 417) for 1%Co-SnO$_2$ NPs. This work is compared with the materials reported in the current literature. As described in Table 1, 0.5%Co-SnO$_2$ NPs are far superior to other materials in terms of response, operating temperature and selectivity.

Repeatability is one of the indispensable sensing characteristics of sensors. Fig. 9(a) exhibits the response transients and deviations for the seven consecutive cycles of 0.5%Co-SnO$_2$ NPs. The sensor is exposed to 30 ppm of formaldehyde at 90 °C, and all 7 responses are close to 160 000. The corresponding response deviation is only 3.8% as shown in the inset, which indicates that the 0.5%Co-SnO$_2$ NPs shows excellent reproducibility to formaldehyde. The linear fit curves between the concentration and response of 0.5%Co-SnO$_2$ NPs and 1%Co-SnO$_2$ NPs are shown in Fig. 9(b). Similarly, the linear fit curves of SnO$_2$ NPs and 2%Co-SnO$_2$ NPs are shown in Fig. 9(c). It is obvious that they are all typical linear relationships, and the response increases linearly as the concentration increases.

To compare the gas-sensing performance of 0.5%Co-SnO$_2$ NPs under different humidity conditions, the gas-sensing behaviors under different humidity are measured. As shown in Fig. 10, it is found that the response decreases slightly from
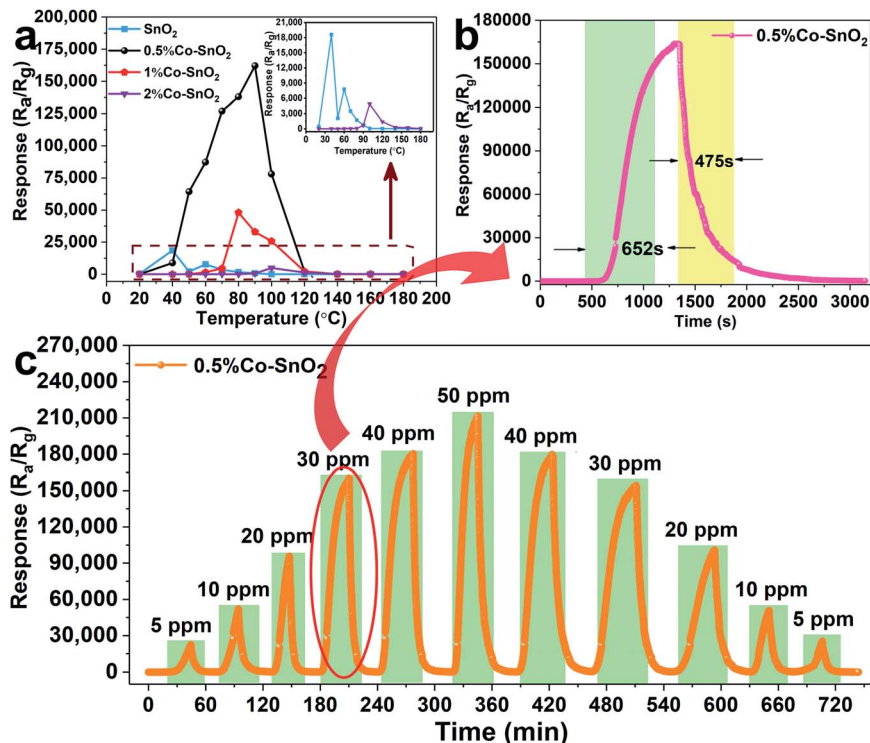
Fig. 6 (a) Response curves of four samples to 30 ppm formaldehyde at 20–180 °C and their partial enlargement (inset), (b) the response and recovery curves of the 0.5%Co-SnO$_2$ NPs at 90 °C to 30 ppm formaldehyde, (c) the response transients of the 0.5%Co-SnO$_2$ NPs at 90 °C and different formaldehyde concentration.
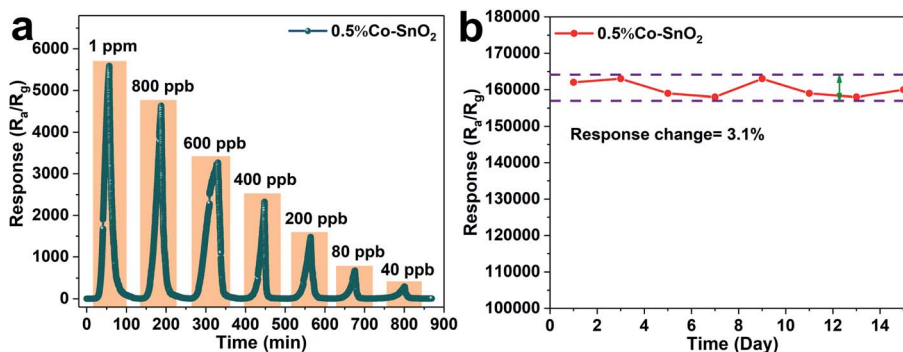

Fig. 7 (a) The response transients of 0.5%Co-SnO$_2$ NPs to ultra-low concentrations of formaldehyde, (b) long-term stability of 0.5%Co-SnO$_2$ NPs to 30 ppm formaldehyde at 90 °C.

dry air to 89% RH. One reason may be that Co doping promotes the dissociation of water vapor on the surface, and the water molecules participates in the surface reaction of the material. For example, the H$^+$ dissociated from the water interacts with the oxygen species of the material.

3.3 Gas-sensing mechanism

At present, the gas-sensing mechanism of metal oxide semiconductor gas sensors is usually explained by the adsorption and desorption of gas on the surface of the materials, which leads to the migration of charge carriers in the semiconductor.[41,42] The SnO$_2$ NPs is a typical n-type semiconductor.

When free oxygen in the air is adsorbed on the surface of SnO$_2$ NPs, it will absorb electrons from its conduction band to form adsorbed oxygen ions (O_2^-, O^-, O^{2-}), thus increasing the resistance of SnO$_2$ NPs. According to the literature, when the temperature is below 100 °C, the main form of oxygen ion is O_2^-. Therefore, the reaction can be expressed as follows:[41,43]

$$HCHO_{(gas)} \rightarrow HCHO_{(ads)} + O_{2(adsorbed)}^- \rightarrow \\ CO_{2(gas)} + H_2O_{(gas)} + e^- \quad (3)$$
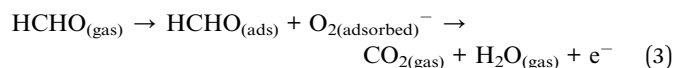
When O_2^- reacts with formaldehyde, electrons are released back into the conduction band of SnO$_2$ NPs, and the resistance of SnO$_2$ NPs decreases. The cross-sectional view of the
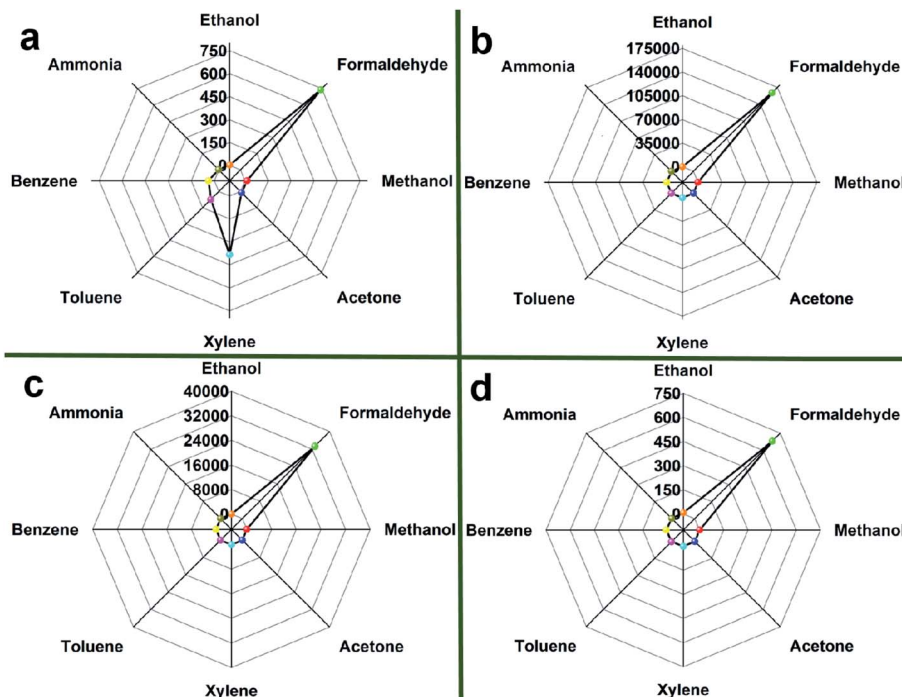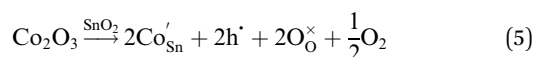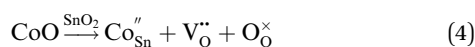
Fig. 8   Responses of (a) SnO$_2$ NPs, (b) 0.5%Co-SnO$_2$ NPs, (c) 1%Co-SnO$_2$ NPs and (d) 2%Co-SnO$_2$ NPs to 30 ppm of various gases at 90 °C.

Table 1   The sensing properties for formaldehyde of 0.5%Co-SnO$_2$ NPs prepared by this work and the performance of other reported materials

Materials	Conc. (ppm)	T (°C)	Response	Ref.
IO-(Ga$_{0.2}$In$_{0.8}$)$_2$O$_3$	100	200	48.8	33
5.0 at% Ni-doped SnO$_2$	50	200	104	34
In$_2$O$_3$/1%Co	10	130	23.2	17
LSCM@SnO$_2$ FITs	5	400	26.5	35
SnO$_2$ NF/NSs	100	120	57	36
6%-Ag/Ni$_{5.0}$In	100	160	123.97	37
3% In$_2$O$_3$–SnO$_2$ nanospheres	100	100	30.7	38
In$_2$O$_3$ hierarchical architecture	100	260	8.6	39
Cu$_2$O quadruple shells	200	120	9.6	40
0.5%Co-SnO$_2$ NPs	30	90	163 437	This work

induction mechanism of SnO$_2$ NPs in air and formaldehyde is shown in Fig. 11(a). The operating mechanism of SnO$_2$ NPs can be intuitively understood by the change of the thickness of the electronic depletion layer on the surface.

When Co is incorporated, Co^{2+} and Co^{3+} ions can replace Sn^{4+} sites in the surface and lattice. According to the Kröger–Vink, the defect reactions are as follows:[44,45]

$$CoO \xrightarrow{SnO_2} Co''_{Sn} + V_O^{\bullet\bullet} + O_O^{\times} \qquad (4)$$

$$Co_2O_3 \xrightarrow{SnO_2} 2Co'_{Sn} + 2h^{\bullet} + 2O_O^{\times} + \frac{1}{2}O_2 \qquad (5)$$

Formula (4) process generates new oxygen vacancies, while formula (5) process generates positively charged holes that will recombine with existing electrons, resulting in an increase in resistance R_a. In n-type semiconductors, higher R_a values are

more likely to have higher responses. However, as the Co content in the sample increases, the grain growth and agglomeration become more and more intense, and the activity of the material decreases greatly. This limits the adsorption and separation of gas on the surface of the material, thereby reducing the gas sensing performance of the sensor, and can be analyzed from the thickness of the depletion layer. In this mechanism analysis, it is assumed that the thickness of the surface depletion layer is approximately the Debye length of the material.[7,46,47] Estimated by the following formula:[7,46,48,49]

$$\lambda_D = \sqrt{\frac{\varepsilon k_B T}{q^2 N_0}} \qquad (6)$$

Here, λ_D represents Debye length, ε is the static dielectric constant, and k_B refers to Boltzmann constant. And, T, q and N_0 are the absolute temperature, the electrical charge of the carrier and the carrier concentration, respectively. The detailed
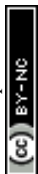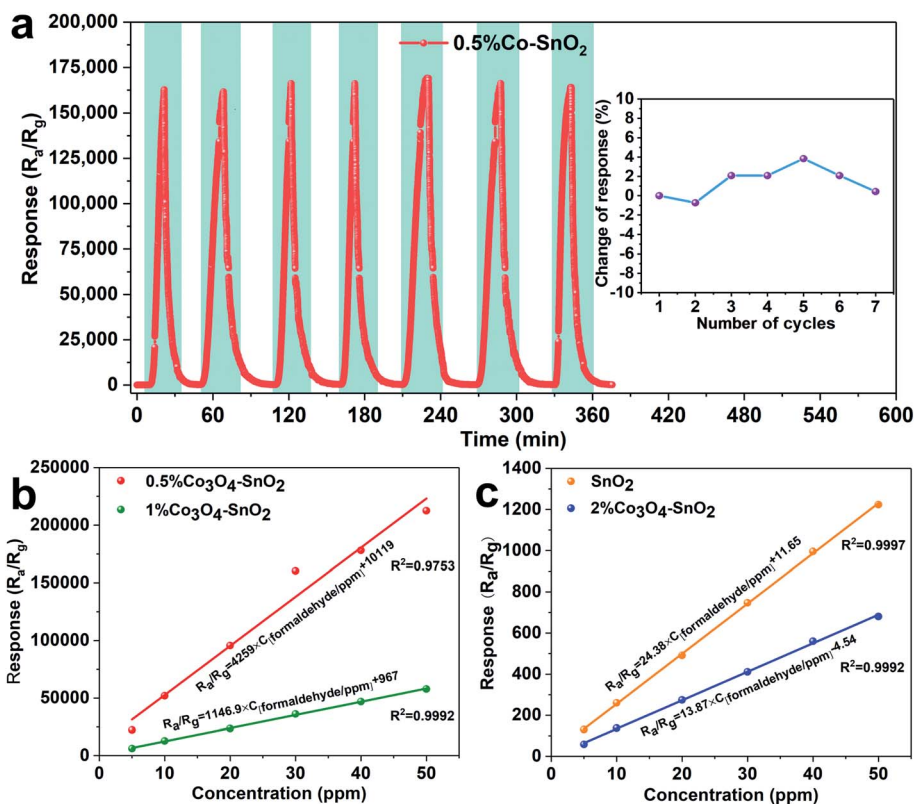
Fig. 9 (a) The seven-time continuous cycle curve of the 0.5%Co-SnO$_2$ NPs to 30 ppm formaldehyde at 90 °C and the change of response after continuous repetition, (b) the linear fitted curves between concentration and response of 0.5%Co-SnO$_2$ NPs and 1%Co-SnO$_2$ NPs, (c) the linear fitted curves between concentration and response of SnO$_2$ NPs and 2%Co-SnO$_2$ NPs.
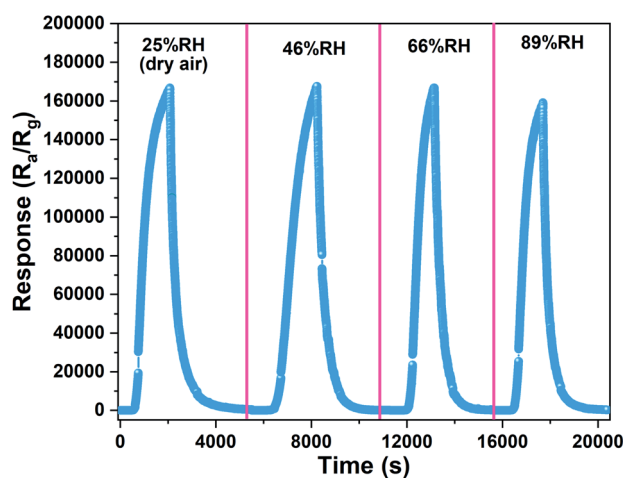

Fig. 10 The dynamic response curve of 0.5%Co-SnO$_2$ NPs under different humidity.

calculation process refers to equation (formula (S3)) in the ESI.† Therefore, the thickness λ_D of the electron depletion layer of SnO$_2$ NPs is 2.55 nm. As can be seen from Fig. 4(a)–(d), the grain size of pure SnO$_2$ NPs is only 2.52 nm, which is extremely close to λ_D. The relationship between the grain size of SnO$_2$ NPs and the thickness of the electronic depletion layer is shown in Fig. 11(b). In general, when the grain size is smaller than the

Debye length, the sensitivity of the metal oxide will increase sharply.[46,50] Consequently, SnO$_2$ NPs show a high response. Although the grain size of 0.5%Co-SnO$_2$ NPs is larger than λ_D, the resistance R_a of the material increases due to the doping of Co, which leads to an increase in response. However, as crystallites grow and agglomerate, the proportion of electron depleted fractions of 1%Co-SnO$_2$ NPs and 2%Co-SnO$_2$ NPs decreases, which leads to a rapid decrease in their sensitivity and response. Moreover, as the size of SnO$_2$ NPs increases, the surface defects and active phases tend to decrease. Thereby, excessive cobalt (p type) doping concentration is not conducive to the detection of formaldehyde gas.

We further performed photoluminescence (PL) and electron paramagnetic resonance (EPR) characterizations which are two typical strategy for identifying oxygen vacancies.[51–53] Fig. 12(a) shows the PL spectra of the as-obtained samples. It can be clearly seen that the emission peaks are located near 350–600 nm, which are due to the rearrangement of holes with two-electron-trapped oxygen vacancies.[54] A stronger peak means more oxygen vacancies. The 0.5%Co-SnO$_2$ sample shows higher intensity, which demonstrates that it has more oxygen vacancies. The large PL intensity of 0.5%Co-SnO$_2$ can be associated with the synergistic effect of Co doping. Furthermore, the excellent response value of 0.5%Co-SnO$_2$ might be due to the increase in oxygen vacancies density, testified by the intensity of the PL peaks. The lattice oxygen is released and the neutral
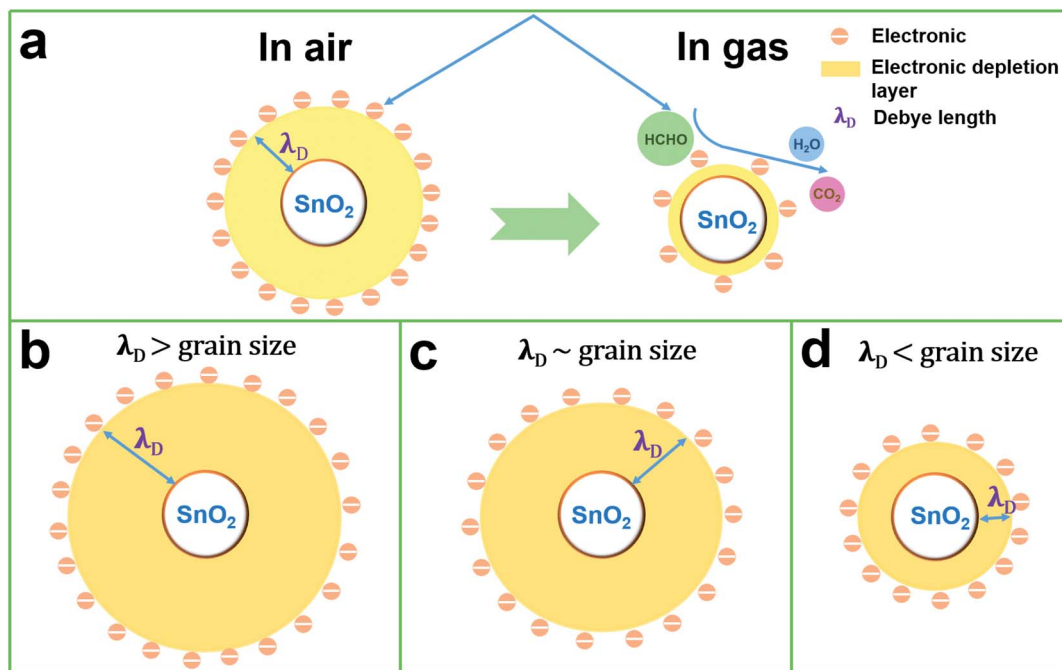
Fig. 11 (a) The cross-sectional view of the sensing mechanism of SnO$_2$ NPs in the presence of air and in formaldehyde; schematic of SnO$_2$ NPs grain size *versus* electron depletion layer thickness, (b) electronic depletion layer (λ_D) > grain size, (c) electronic depletion layer (λ_D) ~ grain size, (d) electronic depletion layer (λ_D) < grain size.

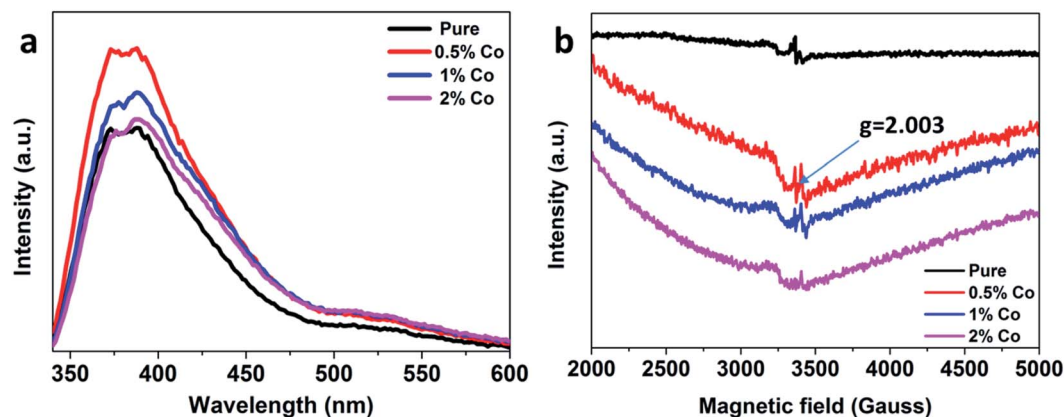
Fig. 12 (a) Photoluminescence spectra and (b) electron paramagnetic resonance spectra of SnO$_2$ NPs, 0.5%Co-SnO$_2$, 1%Co-SnO$_2$ and 2%Co-SnO$_2$.

oxygen vacancy is produced at the initial location, which confirmed the XPS analysis (Fig. 2(d)). Moreover, EPR was used to further prove the existence of the oxygen vacancies (Fig. 12(b)). The symmetric resonance signals of these samples centered at the position ($g = 2.003$) correspond to the oxygen vacancies.[53] The concentration of oxygen vacancies in 0.5%Co-SnO$_2$ is much higher than that of SnO$_2$ NPs. Oxygen vacancies can provide more unpaired electrons for gas-sensing materials, and further bring more adsorbed oxygen ions on the surface, resulting in the enhanced response. EPR results is consistent with the XPS result. It is worth noting that as the amount of Co doping increases, the amount of oxygen vacancies is

significantly reduced, which may be due to the combination of Co atoms and oxygen vacancies.[32]

4. Conclusions

In summary, 0.5%Co-SnO$_2$ NPs were synthesized by simple hydrothermal method, and it is a typical n-type oxide semiconductor, based on which the gas sensor can selectively detect formaldehyde gas at 90 °C. At 90 °C, the response to 30 ppm formaldehyde reaches an astonishing 163 437, and is enhanced with the increase of concentration. In addition, the gas sensing mechanism was analyzed. Due to cobalt doping, the resistance

R_a of SnO$_2$ NPs in the air is improved, and the cobalt doping ratio can be adjusted by Debye length to change the grain size of the sample particles, so that the prepared sample achieves the best performance. The preparation of 0.5%Co-SnO$_2$ NPs is simple and has high performance. Hence, 0.5%Co-SnO$_2$ NPs could considered as a great potential candidate for formaldehyde gas sensors in practical application.

Conflict of Interest

The authors declare no conflict of interest.

Acknowledgements

References

1 A. Allouch, M. Guglielmino, P. Bernhardt, C. Serra and S. Le Calvé, *Sens. Actuators, B*, 2013, **181**, 551–558.

2 G. Bae, I. Jeon, M. Jang, W. Song, S. Myung, J. Lim, S. Lee, H. Jung, C.-Y. Park and K.-S. An, *ACS Appl. Mater. Interfaces*, 2019, **11**, 16830–16837.

3 D. Yang, I. Cho, D. Kim, M. Lim, Z. Li, J. Ok, M. Lee and I. Park, *ACS Appl. Mater. Interfaces*, 2019, **11**, 24298–24307.

4 S. Vallejos, T. Vilic, P. Umek, C. Navío, C. Bittencourt, E. Llobet, C. Blackman, S. Moniz and X. Correig, *Chem. Commun.*, 2011, **47**, 565–567.

5 S. Yang, Z. Song, N. Gao, Z. Hu, L. Zhou, J. Liu, B. Zhang, G. Zhang, S. Jiang, H.-Y. Li and H. Liu, *Sens. Actuators, B*, 2019, **286**, 22–31.

6 X. Liu, N. Chen, B. Han, X. Xuechun, G. Chen, I. Djerdj and Y. Wang, *Nanoscale*, 2015, **7**, 14872–14880.

7 Y. Kwon, H. Na, S. Kang, M. Choi, J. Bang and T. Kim, *Sens. Actuators, B*, 2016, **239**, 180–192.

8 J. Hu, H. Wang, M. Chen, Y. Zhang, X. Zhao, D. Zhang, Q. Lu, J. Zhang and Q. Liu, *Mater. Lett.*, 2019, **263**, 126843.

9 X. Hong, S. Li, R. Wang and J. Fu, *J. Alloys Compd.*, 2018, **775**, 15–21.

10 X. Jiang, Y. Xiong, Z. Zhang, Y. Rong, A. Mei, C. Tian, J. Zhang, Y. Zhang, Y. Jin, H. Han and Q. Liu, *Electrochim. Acta*, 2018, **263**, 134–139.

11 L. Zhu, W. Mengyun, T. Lam, C. Zhang, H. Du, B. Li and Y. Yao, *Sens. Actuators, B*, 2016, **236**, 646–653.

12 J. Du, R. Zhao, Y. Xie and J. Li, *Appl. Surf. Sci.*, 2015, **346**, 256–262.

13 B. Zhang, M. Li, Z. Song, H. Kan, H. Yu, Q. Liu, G. Zhang and H. Liu, *Sens. Actuators, B*, 2017, **249**, 558–563.

14 Y. Wang, Z. Zhao, Y. Sun, P. Li, J. Ji, Y. Chen, W. Zhang and J. hu, *Sens. Actuators, B*, 2017, **240**, 664–673.

15 M. Poloju, N. Jayababu, M. Elayaperumal and M. V. Reddy, *J. Mater. Chem. C*, 2017, **6**, 2662–2668.

16 J. Zhang, F. Xie, L. Yang, S. Guo, Y. Xiong and S. Zhang, *Sens. Actuators, B*, 2021, **340**, 129810–129819.

17 Z. Wang, C. Hou, Q. De, F. Gu and D. Han, *ACS Sens.*, 2018, **3**, 468–475.

18 Y. Wang, H. Li, D. Huang, X. Wang, L. Cai, Y. Chen, W. Wang, Y. Song, G. Han and B. Zhen, *Mater. Sci. Semicond. Process.*, 2022, **137**, 106188–106196.

19 F. Gu, H. Wang, D. Han and Z. Wang, *Sens. Actuators, B*, 2017, **245**, 1023–1031.

20 K. Chen, Y. Zhou, R. Jin, T. Wang, F. Liu, C. Wang, X. Yan, P. Sun and G. Lu, *Sens. Actuators, B*, 2022, **350**, 130807–130817.

21 D. Dutta Pathak and D. Bahadur, *J. Mater. Chem.*, 2012, **22**, 24545–24551.

22 Z. Wang, C. Hou, Q. De, F. Gu and D. Han, *ACS Sens.*, 2018, **3**, 468–475.

23 D. Manikandan and R. Murugan, *Superlattices Microstruct.*, 2015, **89**, 7–14.

24 V. Bonu, A. Das, A. K. Sivadasan, A. Tyagi and S. Dhara, *J. Raman Spectrosc.*, 2015, **46**, 1037–1040.

25 S. Kuchana, M. Vithal, S. Bojja, M. Raja and V. R. Paduru, *J. Phys. Chem. C*, 2009, **113**, 3543–3552.

26 G. Li, X. Wang, L. Yan, Y. Wang and Z. Zhang, *ACS Appl. Mater. Interfaces*, 2019, **11**, 26116–26126.

27 J. Huang, L. Wang, C. Gu, M. Zhai and J. Liu, *CrystEngComm*, 2013, **15**, 7515–7521.

28 R. Nie, J. Shi, W. Du, W.-S. Ning, Z. Hou and F.-S. Xiao, *J. Mater. Chem. A*, 2013, **1**, 9037–9045.

29 W. Tang, W. Xiao, S. Wang, Z. Ren, J. Ding and P.-X. Gao, *Appl. Catal., B*, 2018, **226**, 585–595.

30 L. Chen, D. Jiancai, J. Jia, R. Ran, C. Zhang and X. Song, *ACS Appl. Nano Mater.*, 2019, **2**, 4417–4426.

31 G. Natu, P. Hasin, Z. Huang, Z. Ji, M. He and Y. Wu, *ACS Appl. Mater. Interfaces*, 2012, **4**, 5922–5929.

32 R. S. Ningthoujam, D. Lahiri, V. Sudarsan, H. K. Poswal, S. K. Kulshreshtha, S. M. Sharma, B. Bhushan and M. D. Sastry, *Mater. Res. Bull.*, 2007, **42**, 1293–1300.

33 T. Wang, B. Jiang, Q. Yu, X. Kou, P. Sun, F. Liu, H. Lu, x. Yan and G. Lu, *ACS Appl. Mater. Interfaces*, 2019, **11**, 9600–9611.

34 J. Hu, T. Wang, Y. Wang, D. Huang, G. He, Y. Han, N. Hu, Y. Su, Z. Zhou, Y. Zhang and Z. Yang, *Sens. Actuators, B*, 2018, **263**, 120–128.

35 J.-Y. Kang, J.-S. Jang, W.-T. Koo, J. Seo, Y. Choi, M. H. Kim, D.-H. Kim, H.-J. Cho, W. Jung and I.-D. Kim, *J. Mater. Chem. A*, 2018, **6**, 10543–10551.

36 D. Wang, K. Wan, M. Zhang, H.-J. Li, P. Wang, X. Wang and J. Yang, *Sens. Actuators, B*, 2018, **283**, 714–723.

37 X. Zhang, D. Song, Q. Liu, R. Chen, J. Hou, J. Liu, H. Zhang, J. Yu, P. Liu and J. Wang, *J. Mater. Chem. C*, 2019, **7**, 7219–7229.

38 W. Ge, Y. Chang, V. Natarajan, Z. Feng, J. Zhan and X. Ma, *J. Alloys Compd.*, 2018, **746**, 36–44.

39 S. Wang, J. Cao, W. Cui, L. Fan and D. Li, *Sens. Actuators, B*, 2017, **255**, 159–165.

40 R. Zhang, X. Liu, T. Zhou and T. Zhang, *J. Colloid Interface Sci.*, 2018, **535**, 58–65.

41 M. Chen, Y. Zhang, J. Zhang, K. Li, T. Lv, K. Shen, Z. Zhu and Q. Liu, *J. Mater. Chem. C*, 2018, **6**, 6138–6145.

42 Y. Zhang, Q. Rong, J. Zhao, J. Zhang, Z. Zhu and Q. Liu, *J. Mater. Chem. A*, 2018, **6**, 12647–12653.

43 G. Li, Z. Cheng, Q. Xiang, L. Yan and X. Wang, *Sens. Actuators, B*, 2018, **283**, 590–601.

44 G. Brankovic, Z. Brankovic, M. Davolos, M. Cilense and J. Varela, *Mater. Charact.*, 2004, **52**, 243–251.

45 M. Punginsang, A. Wisitsoraat, A. Tuantranont, S. Phanichphant and C. Liewhiran, *Sens. Actuators, B*, 2015, **210**, 589–601.

46 Q. Xu, Z. Zhang, X. Song, S. Yuan, Z. Qiu, x. Hongyan and B. Cao, *Sens. Actuators, B*, 2017, **245**, 375–385.

47 G. Korotcenkov, *Mater. Sci. Eng., R*, 2008, **61**, 1–39.

48 A. Katoch, S.-W. Choi, G.-J. Sun and S. Kim, *J. Mater. Chem. A*, 2013, **1**, 13588–13596.

49 F. Qu, J. Liu, Y. Wang, S. Wen, Y. Chen, X. Li and S. Ruan, *Sens. Actuators, B*, 2014, **199**, 346–353.

50 G. Korotcenkov, *Sens. Actuators, B*, 2005, **107**, 209–232.

51 H. Bi, L. X. Zhang, Y. Xing, P. Zhang, J. J. Chen, J. Yin and L. J. Bie, *Sens. Actuators, B*, 2021, **330**, 129374–129385.

52 L. X. Zhang, G.-N. Li, Y.-Y. Yin, Y. Xing, H. Xu, J. J. Chen and L. J. Bie, *Sens. Actuators, B*, 2020, **325**, 128805–128818.

53 G. N. Li, X. Y. An, L. X. Zhang, Y. Xing and L. J. Bie, *Mater. Lett.*, 2022, **307**, 131026–131029.

54 J. Bao, X. Zhang, B. Fan, J. Zhang, M. Zhou, W. Yang, X. Hu, H. Wang, B. Pan and Y. Xie, *Angew. Chem., Int. Ed. Engl.*, 2015, **54**, 7399–7404.